Large Eddy Simulation of Micro-Riblet Performance Under Upstream Flow Separation

Y. Wang[1,2], Z. Sun[1], S. Ju[1], D. Guo[1], B. Yin[1] and G. Yang[1]

**[1]Key Laboratory for Mechanics in Fluid Solid Coupling Systems,
Institute of Mechanics, Chinese Academy of Sciences
Beijing, China
[2]School of Engineering Science, University of Chinese Academy
of Sciences, Beijing, China**

Abstract

Micro-riblets are effective for reducing drag in turbulent layers. Flow separation is a prevalent flow phenomenon in transport. However, the precise drag reduction performance of riblets downstream of a flow separation remains unclear. An inclined forward step model is proposed to investigate the interaction between riblet and upstream flow separation. The large eddy simulation method is applied to simulate the flow over geometries with different step angles and riblet positions. The results show that the riblet downstream of a flow separation still reduce drag and have two characteristics, with two distinct behaviours. Firstly, drag reduction rises with separation intensity; a step angle increase from 0 to 30 degree boosts drag reduction from 9.5% to 12.6%. This is due to intensified Q2 motions enhancing riblet effects. Secondly, the position of the riblets has a significant impact on the pressure drag. Riblets close to the point of separation enhance flow separation, altering the surface pressure distribution and thus increasing the resistance. The precise performance of riblets under complex flow conditions is are important for their practical engineering application on the train.

Keywords: high speed train, flow control, aerodynamic drag, turbulent boundary layer, micro structures, computational fluid dynamics.

1   Introduction

A Skin-friction drag is a key factor in flow resistance and affects energy costs. Reducing this drag is vital in fluid dynamics engineering. Shark skin microstructures,

known to decrease flow resistance, have inspired the creation of riblets—micro-grooves aligned with the flow direction. These riblets are a promising technology for reducing drag passively[1]. Early pioneering studies obtained a friction drag reduction of up to 8% when the spacing of the riblet was less than 25 wall units, proving the riblet's validity[2]. Bechert et al.[3] further optimized riblet shapes, achieving a 9.9% drag reduction.

The mechanism behind riblets' drag reduction has been widely studied. Based on viscous analyses, Luchini et al.[4] explained the mechanism in Stokes flow. Their explanation is based on the distinction between the protrusion height of cross-flow and that of streamwise flow. Here, Protrusion height referred to the vertical distance between the tip of a riblet and the origin of the Stokes flow. Their analysis suggested that riblets hinder cross-flow, a factor that is considered critical in the turbulence regeneration cycle. Consequently, this hindrance reduces the intermixing of streamwise momentum, leading to a reduction in frictional drag. Furthermore, the interaction between the riblet and the quasi-streamwise vortices in the turbulent boundary layer is also considered to be the reason for the drag reduction. Lee & Lee[5] drew the conclusion, supported by particle tracking velocimetry (PTV) measurements, that riblets limit the regeneration of quasi-streamwise vortices. Choi et al.[6] performed Direct Numerical Simulation (DNS) for a channel flow with a riblet surface and reported that the riblet affected ejection and sweep events and inhibited quasi-streamwise vortices in the region near the wall. Goldstein et al.[7] reported riblets reduce RMS velocity fluctuations, minimizing interaction with larger turbulence scales. Additionally, García-Mayoral & Jiménez[8] proposed the square root of riblet area, $l_G^+ = \sqrt{A_G^+}$, as a better performance indicator, with an optimal range of 9.7-11.7 for various profiles.

Micro-riblets are recognized as an effective flow control method in transportation, particularly for their drag reduction capabilities. The aerospace sector has shown consistent interest in riblets for drag reduction. Viswanath[9] assessed tests showing 3M riblets' effectiveness on various aircraft parts across speeds and Mach numbers. Kurita et al.[10] explored paint riblets' friction reduction via flight tests. Zhang et al.[11] used simulations to analyze riblets' drag reduction on low-speed airfoils.

Moreover, the riblet is receiving heightened attention in the region of high-speed trains where frictional drag can account for more than 40% of the total drag. However, it is imperative to recognize that the boundary layer on trains and cars is different from that of flat plates or airfoils. The presence of blunt bodies, such as vehicle fronts, leads to flow separation and significant unfavorable pressure gradients, thereby altering the downstream turbulent structures. Studies on riblets under varying pressure gradients offer mixed results. K.-S. Choi[12] found no change in skin friction with pressure gradients, while Truong & Pulvin[13] observed reduced riblet effectiveness under

stronger gradients. Conversely, Debisschop & Nieuwstadt[14] saw nearly double the drag reduction, and Klumpp et al.[15] reported increased drag reduction in adverse gradients. Boomsma & Sotiropoulos[16] noted consistent drag reduction across different gradients. In addition, the impact of flow separation on riblets' performance remains underexplored. Understanding the behavior of riblets under flow separation conditions is essential for their application in the transportation industry.

To explore the complex interaction between upstream flow separation and riblet-induced drag reduction in turbulent boundary layers, the current study introduces an innovative inclined forward step model with riblets positioned downstream of the step. Gases traversing the forward step at different angles, resulting in different levels of flow separation. A series of large eddy simulations are applied to calculate the proposed inclined forward step model with different step angles and riblet positions. The remainder of this paper is organized as follows: Section 2 describes the inclined forward step model and the numerical method. Subsequently, A series of large eddy simulations are performed on the forward step model, encompassing varying inclinations and riblet positions in Section 3. First, the mechanism behind riblet-induced drag reduction is elucidated. Then, the influence of upstream flow separation on riblet performance is discussed. Finally, within the same section, the study extends to the impact of riblet positions on the upstream flow separation. Conclusive insights and deductions are summarized in Section 4.

2   Methods

2.1 Computational Domain and Grid Configuration

Figure 1 illustrates the geometric configuration of the computational domain. The three primary directions are designated as streamwise (x), vertical (y), and spanwise (z), each associated with the respective velocity components (u, v, and w). The notation superscript '+' signifies quantities scaled by the friction velocity ($u_\tau = \sqrt{\tau_w/\rho}$) and the kinematic viscosity (ν), where τ_w denotes the wall shear stress and ρ represents the fluid density. The reference length, δ, corresponds to the boundary layer thickness at $x=10\delta$ in the 20° step case without riblets. The spanwise extent of the computational domain is denoted as W, approximately measuring 560 wall units. The computational domain's vertical extent at the outlet is defined as $H = 30\delta$. The solid wall can be divided into three sections: the turbulence development section, the inclined forward step section, and the designated working section. The working section is composed of both a flat segment and a riblet segment. The Reynolds number based on the average velocity (U_∞) at the inlet and the length of turbulence development section (L_{dev}) is $Re_L = 5 \times 10^5$. This substantial value ensures the establishment of a fully developed turbulent boundary layer. The angle of the forward step, θ, spans four variations: $\theta = 0°$, 10°, 20°, and 30°. Concerning the working section, the cumulative length of the flat segment, L_{flat}, and riblet segment, L_{riblet},

amounts to 50δ. Notably, L_{flat} is varied in different cases to investigate the effect of the riblet position on the flow structure.

Within the working section, 40 riblets are arranged in a side-by-side configuration along the spanwise direction. The zoom-in drawing of riblet parameters is shown in the top left part of Figure 1. The spanwise width of each riblet (s^+) measures 14, while the height-over-width ratio ($\frac{h^+}{s^+}$) is fixed to 0.6. The square root of the riblet cross-sectional area ($\sqrt{A_G^+}$) is 10.8, a value aligning with the optimal range as determined by García-Mayoral & Jiménez[8]. They further noted that the optimal geometry configuration is blade type structure which is adopted in the present research.
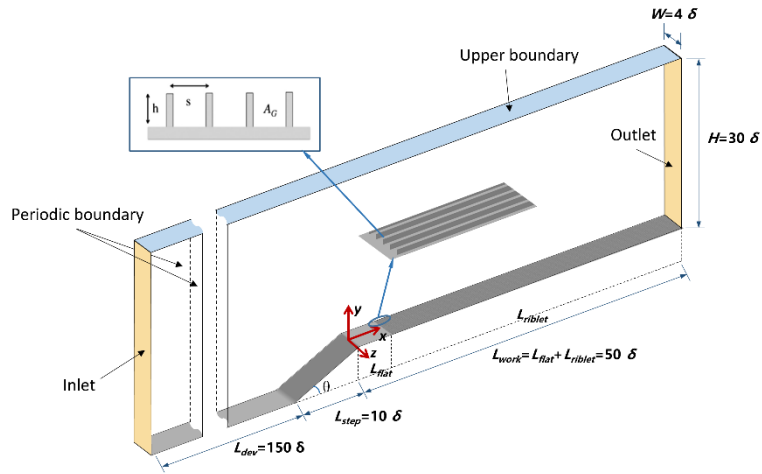
Figure 1: Sketch of the computational domain with its local enlargement to illustrate the parameters of the riblets geometry.

The computational grid has a dimension of $594 \times 800 \times 200$ in streamwise (x), wall-normal (y), and spanwise (z) directions, respectively. In the x-direction, the cell size is non-uniformly distributed starting at $\Delta x^+ \approx 14$ near the upper edge of the step and growing to $\Delta x^+ \approx 30$ at the inlet and outlet of the computational domain. Meanwhile, in the z direction, a consistent cell size is maintained, characterized by a resolution of $\Delta z^+ \approx 0.7$. Within the wall-normal (y) direction, the first grid interval is set to be $\Delta y_{first}^+ \approx 0.7$ to capture the small-scale features inherent in turbulence.

2.2 Numerical Algorithm and Validation

The governing equations are the unsteady incompressible Navier-Stokes equations, which are discretized by the method of finite volume in CFD simulations. The Large-eddy simulations (LES) are conducted to solve the equations. The convective flux term is discretized by a bounded central-differencing scheme, which provides a good

compromise between accuracy and robustness[17]. For the diffusion terms, a second-order upwind scheme is employed. Meanwhile, to approximate the transient term, the Euler implicit second-order scheme is implemented. A dual time-stepping technique is used to solve the unsteady flow equations, where the internal iteration steps are carefully tuned to ensure that the residuals have a decrease of at least one order of magnitude within each time step. The time step Δt is chosen small enough to ensure that the Courant-Friedrichs-Lewy (CFL) number is generally less than 1. Importantly, the computed time span exceeds 15 flow-through times, symbolized as $(L_{dev} + L_{step} + L_{flat} + L_{riblet})/U_\infty$

The Wall-Adapting Local-Eddy Viscosity (WALE) subgrid scale model [18] is employed for turbulence closure. This model can provide accurate scaling near walls without using a dynamic procedure. In the near-wall region, the WALE model is recognized for its competence in accurately predicting flow behavior [18], [19], [20]. Validation of the predictive power of the WALE model can be seen in the simulations performed by Temmerman et al.[21] on a channel with hilly topography and periodic constrictions, where the model is compared with Direct Numerical Simulation. In addition, the effectiveness of the WALE model in handling complicated flow problems has been demonstrated[24,25,26].

To validate the capability of the numerical method to effectively simulate turbulent boundary layers with riblets, a simulation of a channel flow is conducted. Following the setup outlined by Choi et al.[6] , the upper wall is a flat plate, while the lower wall integrates riblets, as shown in Figure 2. There are 24 riblets with width of $s^+ = 20$ in the computation. The Reynolds number based on the centerline velocity (U_l) of a laminar parabolic profile with the same volume flux and the channel half height (h) is $Re_h = 4200$. The computational domain extends $2\pi \times 2 \times 1.39h$ in the streamwise, wall-normal and spanwise direction. It is resolved by $96 \times 128 \times 360$ grid points. The accuracy of the numerical method is confirmed by the DNS data of [6] and the LES data of [11]. The drag coefficient C_d is defined below:

$$C_d = \frac{2F_x}{\rho_0 U^2 S} \tag{1}$$

Here, the force vector components F_x is computed by integrating all the normal and shear stresses over the objective along the streamwise direction. The reference velocity is the U_l, and S is the wetted area of the flat plate. Table 1 compares the time-averaged drag coefficients. The results of the present study are very close to the results of the reference DNS and LES data. Comparing the difference of time-averaged drag between the riblet wall and the flat plate, the drag reduction rate is 6.2%, closely aligning with the reference DNS result of 6.4%. Furthermore, Figure 3 shows the time-averaged velocity profile from the riblet to the flat wall. The velocity profiles of the riblet valley and the riblet tip are both presented in the figure. The LES results are in good agreement with the DNS data.

5

	C_d of flat plate	C_d of riblet wall	Drag reduction
Present study	0.00369	0.00346	6.2%
[6]	0.00367	0.00343	6.4%
[11]	0.00370	0.00344	6.9%

Table 1. Drag coefficients for the LES in present study, the LES from [11] the DNS from [6]
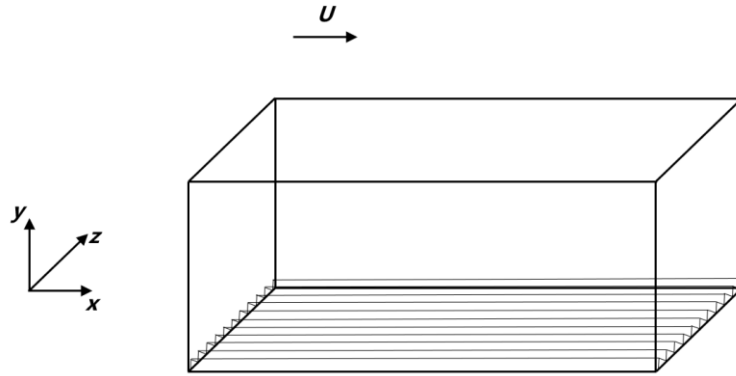
Figure 2: The computational domain for numerical validation.
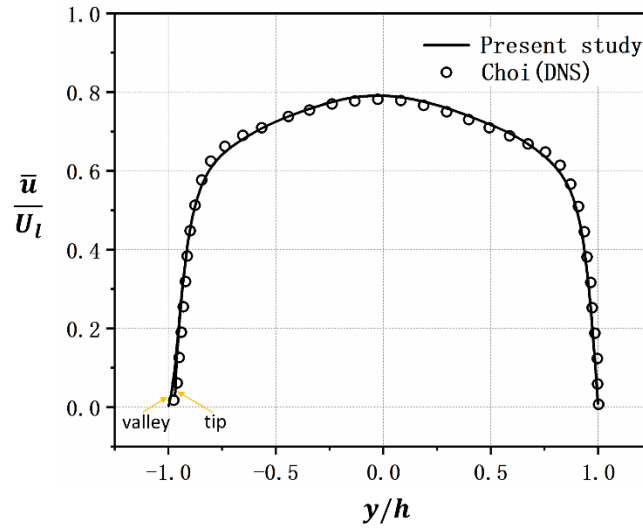
Figure 3: Time-averaged velocity profile from the riblet to the flat wall in the channel.

3   Results

Having established the simplified geometric model and validating our numerical methodology, our investigation pivots to the intricate interaction between upstream flow separation and downstream riblet-induced drag reduction. This is achieved by

6

systematically varying the angle of the step θ and the distance of the riblets from the trailing edge of the step L_{flat}. A comprehensive summary of our simulation permutations is presented in Table 2, including the model parameters and results of resistance. The quantification of drag reduction (DR) is expressed through the following equation:

$$DR = \frac{C_{d,clear} - C_{d,riblet}}{C_{d,clear}} \times 100\% \qquad (2)$$

Where C_d is the drag coefficient aligned with the streamwise direction which has been defined in Equation (1). The subscript "clear" represents the model without riblets and the subscript "riblet" represent the model with riblets. For the C_d of working section, the reference area S corresponds to the projected area in the wall-normal direction within the streamwise interval $x \in [0, 50\delta]$. For the C_d of step, the S is defined by the projection of step along the streamwise direction.

A comparison of the drag coefficient (C_d) shows that riblets reduce the frictional resistance even when the upstream flow experiences separation. Intriguingly, when the distance (L_{flat}) remains constant but the step angle (θ) varies across models, the DR of the working section varies. This observation leads to the hypothesis that the performance of riblets is closely linked to upstream flow conditions. There is also an interesting phenomenon where riblets seem to cause an increase in step resistance. The following section takes a comprehensive exploration of these 2 phenomena. Firstly, a detailed analysis of the mechanism underlying the riblet-induced resistance reduction under typical operating conditions is given in Section 3.1. Subsequently, in Section 3.2, we discuss the effect of upstream separation on the downstream performance of riblets. The complex interaction between riblet positioning, pressure distribution and the drag coefficient (C_d) of the step is examined in Section 3.3.

Case	Riblet / Clear	Step angle θ	L_{flat} (δ)	C_d of working section	DR of working section	C_d of step
1	Clear	0°	/	0.00417	/	/
2	Riblet	0°	/	0.00377	9.5%	/
3	Clear	10°	/	0.00413	/	0.0595
4	Riblet	10°	0	0.00352	14.9%	0.0670
5	Riblet	10°	2.5	0.00352	14.9%	0.0617
6	Riblet	10°	5	0.00360	12.9%	0.0610
7	Riblet	10°	7.5	0.00369	10.6%	0.0606
8	Riblet	10°	10	0.00370	10.4%	0.0596
9	Clear	20°	/	0.00413	/	0.0716
10	Riblet	20°	0	0.00320	22.5%	0.0857

11	Riblet	20°	2.5	0.00326	21.1%	0.0745
12	Riblet	20°	5	0.00351	15.2%	0.0735
13	Riblet	20°	7.5	0.00359	13.3%	0.0725
14	Riblet	20°	10	0.00362	12.4%	0.0716
15	Clear	30°	/	0.00340	/	0.1301
16	Riblet	30°	0	0.00233	31.4%	0.1438
17	Riblet	30°	2.5	0.00242	28.8%	0.1326
18	Riblet	30°	5	0.00273	19.8%	0.1324
19	Riblet	30°	7.5	0.00287	15.7%	0.1302
20	Riblet	30°	10	0.00297	12.6%	0.1301

Table 2: Model parameters and drag coefficients for all simulation cases

3.1 Flow Statistics of Drag Reduction by Riblet

This section analyses the mechanism of riblet-induce drag reduction through a comprehensive investigation involving turbulence statistics and quadrant analysis. This section, dedicated to the meticulous scrutiny of this mechanism, engenders a comprehensive juxtaposition of flow fields. To this end, a typical case, Case 14, characterized by a step angle of 20° and an L_{flat} value of 10δ, is selected. Case 9, which is the clear model without riblet, is used as a control benchmark against case 14. Compared to case 14, the *DR* of the working section of Case 9 is 12.4% which is higher than that of the flat plate model (case 2). The C_d of the step in Case 14 is found to be identical to that in Case 9, which suggests that the presence of riblets in this case has no discernible effect on the intensity of flow separation. This strategy ensures that the only factor affecting the drag reduction (*DR*) of the working section remains the interaction between the riblets and the prevailing turbulent structures.

3.1.1 Turbulence statistics

To elucidate the underlying physical mechanisms for riblet-induced drag reduction, turbulence statistics from the turbulent flow at several streamwise positions are presented. In high Reynolds number flows, the wall frictional resistance exhibits a strong correlation with the Reynolds shear stress. In the context of turbulent flow within a channel bounded by two infinite parallel flat plates under the influence of a constant pressure gradient, the streamwise mean motion equation yields the following expression:

$$\mu \frac{dU}{dy} - \rho \langle u'v' \rangle = \tau_\omega \left(1 - \frac{y}{\delta}\right) \tag{3}$$

8

Where y represents the vertical direction, δ is the half height of the channel, τ_ω denotes the wall shear stress. The wall friction coefficient is defined as $C_f = \tau_\omega/(\rho U_{AVG}^2)$, where U_{AVG}^2 stands for the average velocity of the cross section. The C_f can be obtained by integrating Eq. (3).

$$C_f = \frac{3}{Re_{AVG}} - \frac{3}{\delta^2 U_{AVG}^2} \int_0^\delta (\delta - y) \langle u'v' \rangle \mathrm{d}y \qquad (4)$$

Where $Re_{AVG} = U_{AVG}\delta/v$. The first term on the right-hand side of the above equation is related to viscosity and corresponds to the wall friction coefficient for laminar flow. The second term represents the integral of the Reynolds shear stress, which stands for the main contributor to wall friction in highly turbulent flows. Comparison of the Reynolds shear stress distribution helps to comprehend the mechanism of riblet-induced drag reduction. Figure 4 illustrates the variation of Reynolds shear stress ($\overline{u'v'}$) against wall distance at several streamwise positions. The variations in the shear stress caused by the riblets are similar to those observed in normal stress. Apparently, the Reynolds shear stress is attenuated in proximity to the riblet. Moreover, the peak Reynolds shear stress of the riblet model is significantly lower than that in the clear model. This observation indicates that the process of momentum transportation is suppressed by the riblet.
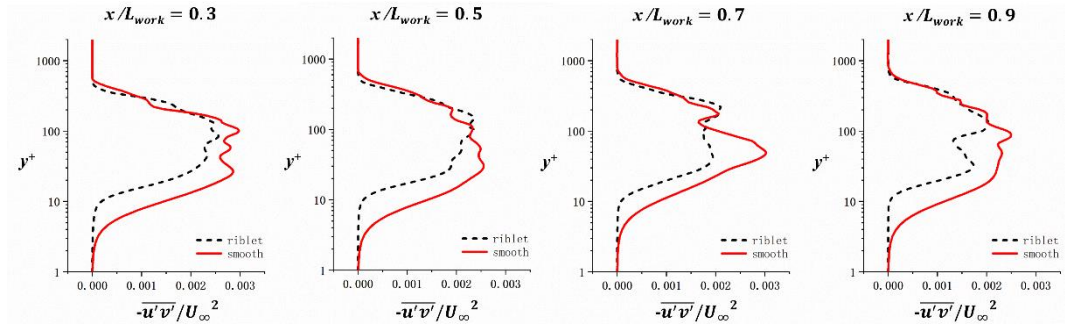
Figure 4: The profile of the non-dimensional Reynolds shear stress $-\overline{u'v'}/U_\infty^2$ at streamwise positions of $x/L_{work} = 0.3, 0.5, 0.7, 0.9$.

3.1.2. Quadrant analysis of Reynolds shear stress

An in-depth analysis of momentum transport and the generation of turbulent kinetic energy within the near-wall region can be achieved through quadrant analysis of Reynolds shear stress. The signs of the streamwise velocity fluctuations (u') and the wall-normal velocity fluctuations (v') are recognized to contain useful information of boundary layer flow. Velocity fluctuations are categorized into four distinctive groups: Q1 ($+u'$, $+v'$), Q2 ($-u'$, $+v'$), Q3 ($-u'$, $-v'$), and Q4 ($+u'$, $-v'$), which were called the quadrants of the Reynolds shear stress plane [25]. It worth noting that Q2 and Q4 are gradient-type motions, which are clearly related to the ejection and sweep

events in the near-wall region, respectively. The term gradient-type motion is used to indicate vertical momentum fluxes due to fluid elements moving up and down having a streamwise momentum that is less or greater than the local mean streamwise momentum, respectively. It is often assumed that Q2 and Q4 motions make the largest contributions to the Reynolds shear stress, whereas the Q1 and Q3 motions signify outward and inward interactions.

A thorough investigation into the primary physical processes contributing to the attenuation in Reynolds shear stress induced by riblets is conducted through quadrant analysis. Figure 5 shows the distribution of the motions across the four quadrants at the height of $y^+ = 30$. Evidently, the peak of each quadrant is located at approximately $0.05\,L_{work}$, which aligns with the center of the separation region following the step. Focusing specifically on the region over the riblet [$0.2L_{work}$, $1.0L_{work}$], Q2 and Q4 contribute considerably more to the turbulent shear stress than Q1 and Q3. Q1 and Q3 are small and nearly identical for both the clear model and the flat plate. As can be seen, Q2 decreases significantly over the riblet, while Q4 shows no obvious change. Consequently, the ejection motions in turbulence boundary layer are effectively suppressed by the presence of riblets, which emerge as the primary factor behind the reduction in Reynolds shear stress. Ejection motions, characterized by the expulsion of near-wall fluid, account for much of the outward vertical transport of momentum and thus for the high frictional resistance in turbulent flow.
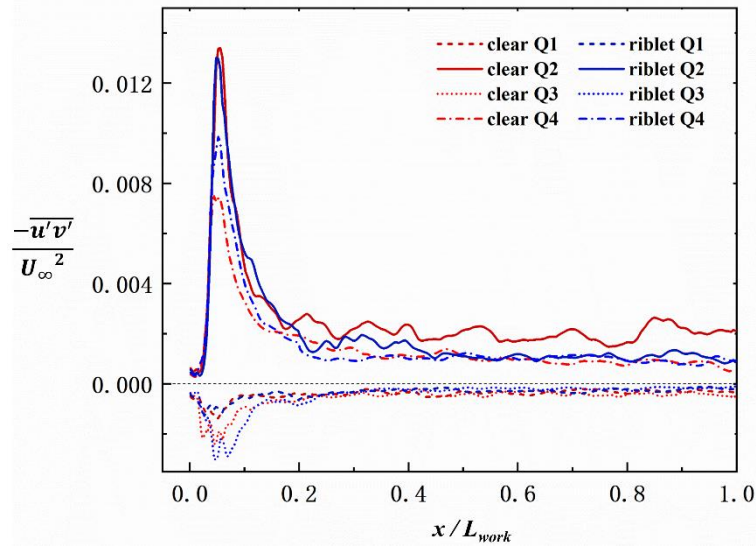
Figure 5: The quadrant analysis of Reynolds shear stress for the clear model and the riblet model at $y^+ = 30$.

3.2. Influence of Separation on Downstream Riblets Performance

Table 2 reveals distinct variations in the drag reduction (DR) of the working section among models featuring different step angles (θ) but a consistent L_{flat}. Therefore, the performance of riblets is influenced by the strength of the upstream separation. This section analyzes Case 2, Case 8, Case 14, and Case 20, where the step angles are 0°, 10°, 20°, and 30°, respectively, while maintaining $L_{flat} = 10\delta$. Additionally, for comparative purposes without riblets, Case 1, Case 3, Case 9, and Case 15 are studied correspondingly. The reason for choosing the model with $L_{flat} = 10\delta$ is the same as in section 3.1. This choice ensures that riblet performance is the sole factor impacting the drag reduction within the working section. Figure 6 illustrates the DR of the working section for cases with different step angles. Notably, as the step angle increases, the DR increases from 9.5% to 12.6%. This rise in DR is linked to the augmentation of flow separation caused by larger step angles.

Section 3.1 highlighted the influence of riblets on the turbulence structure by suppressing ejection motions which can be represented by the Q2 quadrant of Reynolds shear stress. Consequently, the distributions of the Q2 quadrant motions along the flow direction at $y^+ = 30$ in cases with different step angles are shown in Figure 7. Evidently, a higher Q2 motion emerges in the near-wall region following passage through a step with a large angle. This augmentation in ejection motions within the boundary layer is attributed to the stronger flow separation upstream. The wake flows resulting from separation may influence both turbulence intensity and structure within the boundary layer. Moreover, riblets exhibit more pronounced Q2 suppression in the case with a larger step angle.

To quantify the Q2 alterations, Table 3 counts the mean value of Q2 at $y^+ = 30$, the Q2 proportion within the shear stress, and the Q2 reduction attributed to riblets. Q2 proportion is the percentage of components with negative streamwise velocity fluctuations and positive wall-normal velocity fluctuations at the same time in the Reynolds shear stress integration process. Q2 reduction is the ratio of reduction in the mean value of Q2 for the riblet model compared to the smooth model with the same step angle. As the step angle increases, not only does the mean value of Q2 rise, but the proportion of Q2 within Reynolds stress also increases. Correspondingly, the Q2 reduction achieved by riblets improved from 23.7% to 43.8%. This variation in Q2 elucidates the rationale behind the DR enhancement associated with increasing step angles.

11
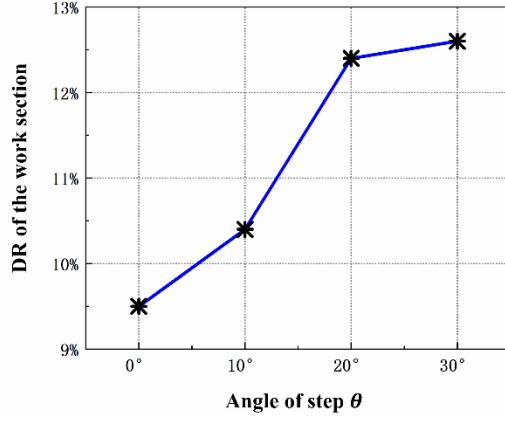
Figure 6: The *DR* of the working section varies with the angle of step θ.
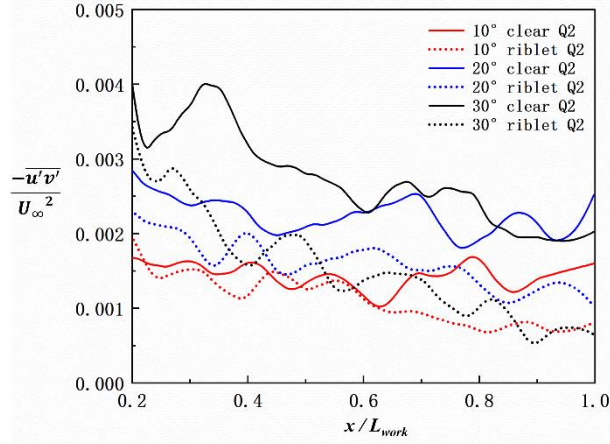
Figure 7: The Q2 quadrant of Reynolds shear stress for the cases with different step angles at $y^+ = 30$.

Case	Riblet / Clear	Step angle θ	DR of working section	Mean value of Q2	Q2/Reynolds shear stress	Reduction of Q2
3	Clear	10°	/	0.00144	72.2%	/
8	Riblet	10°	10.4%	0.00110	71.6%	23.7%
9	Clear	20°	/	0.00205	88.1%	/
14	Riblet	20°	12.4%	0.00123	71.1%	39.9%
15	Clear	30°	/	0.00271	98.9%	/
20	Riblet	30°	12.6%	0.00152	78.9%	43.8%

Table 3: Mean values of Q2 for the cases with different step angles at $y^+ = 30$.

12

3.3 Effect of riblets position on pressure distribution and pressure drag

As well as reducing frictional resistance, the riblets can also affect the distribution of pressure, altering the pressure drag of the forward step. Table 2 highlights that the position of riblets is the primary factor in determining the pressure distribution. To explain in detail the effect of the riblet position, the flow fields of Cases 10, 11, 12, and 14 are analyzed in this section. These cases entail L_{flat} value of 0δ, 2.5δ, 5δ and 10δ respectively, all featuring a step angle of 20°. Case 9 without riblet is the corresponding simulation for comparison. Figure 8 presents the drag coefficient (C_d) of the step across cases with varying L_{flat}. Notably, when the riblet is positioned immediately behind the step, the drag of the step is maximized, increasing by 19.7% compared to the clear model. With an increase in L_{flat}, the drag of the step decreases. Until reaching $L_{flat} = 10\delta$, the drag of the step aligns with that observed in the clear mode.
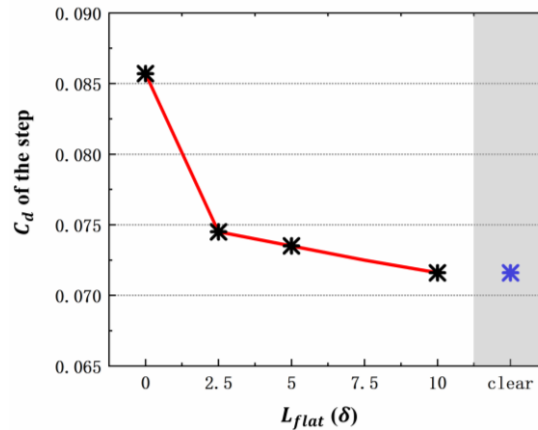
Figure 8: The drag coefficient C_d of step varies with the L_{flat}.

Figure 9 illustrates the distribution of time-averaged pressure on both the step and the working section. At the leading edge of the step, a positive pressure zone emerges due to the flow's deceleration, while the flow accelerates and separation occurs near the trailing edge of the step, resulting in a pronounced negative pressure zone. Comparing Figure 9 (a) and (b), the riblet positioned to the step significantly weakens the negative pressure zone, resulting in increased pressure drag on the step. This phenomenon is not evident after $L_{flat} > 2.5\delta$. For a quantitative evaluation of the influence of riblets position on pressure distribution, Figure 10 illustrates the pressure distribution along the flow direction on the centerline of the step. The model with $L_{flat} = 0$ exhibits overall higher surface pressure compared to the clear model. Specifically, the pressure is elevated by 400 Pa near the trailing edge of the step. Models with $L_{flat} = 2.5\delta$, 5δ, 10δ display pressure profiles similar to the clear

13

model. The locally enlarged graphs reveal slight pressure increase near the trailing edge of the step for models with $L_{flat} = 2.5\delta,\ 5\delta$. Differences in surface pressure distribution align cohesively with variations in the pressure drag of the step.
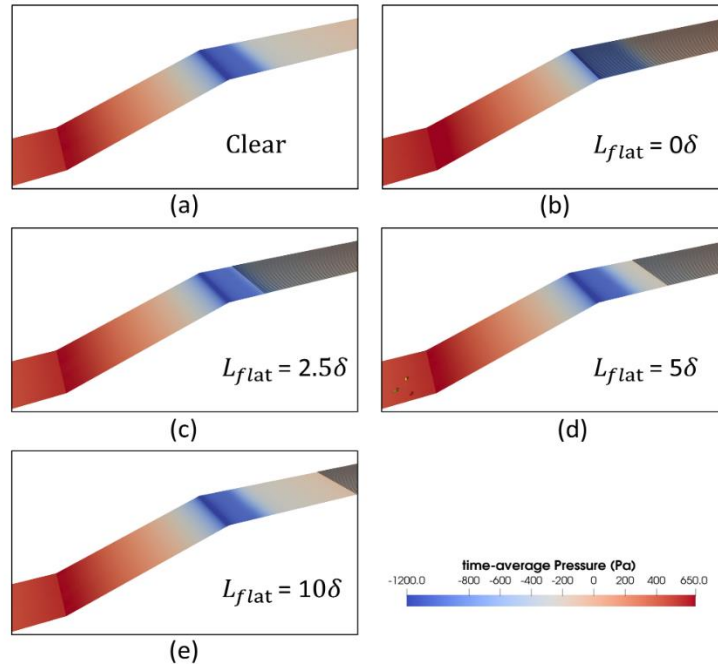
Figure 9: Contours of the time-averaged pressure on the step and the working section: (a) case without riblet; (b) case with L_{flat} of 0; (c) case with L_{flat} of 2.5δ; (d) case with L_{flat} of 5δ; (e) case with L_{flat} of 10δ.
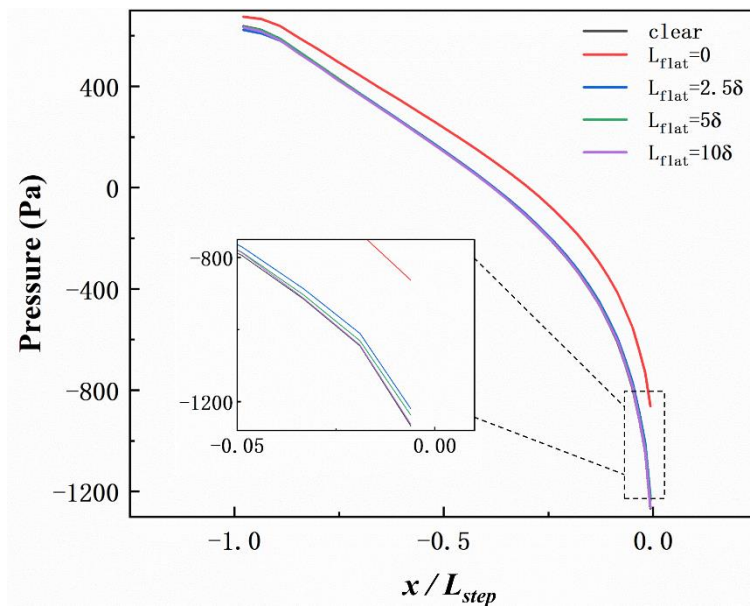
Figure 10: Distribution of time-averaged pressure on the centerline of the forward steps.

The time-averaged streamlines colored with velocity values at the mid-plane for both the case without riblet and cases with varying L_{flat} are shown in Figure 11. In all cases, flow separation is observed from the trailing edge of the step. A flow separation bubble appears in the separated shear layer, and the separated flow reattaches to the working section downstream. In the case with L_{flat} of 0, the region of flow separation is the largest. As L_{flat} increases, the flow separation region decreases, and the flow separation region becomes as large as that of the clear model when $L_{flat} = 10\delta$. The reattachment length(R) is defined as the distance between the flow separation point and the reattachment point to quantify the size of the flow separation region[28,29]. The reattachment lengths for these cases are listed in Table 4. The R value for the case with L_{flat} of 0 is 4.84δ, signifying a 64.6% increase compared to the clear model. This enhanced flow separation can potentially be attributed to the presence of riblets close to the step, disturbing high-velocity fluid and augmenting flow instability. The increased flow separation in turn leads to reduced flow velocity at the trailing edge of the step, culminating in increased pressure on the step. Table 4 shows that the reattachment length and the drag coefficients of step for the $L_{flat} = 10\delta$ are consistent with the model without the riblet. This indicates a critical length whose effect on flow separation is negligible once the distance between the riblet and the separation point is greater than the critical length. This indicates the existence of a critical length which determines whether the effect of the riblet on flow separation can be neglected. The critical length is approximately 160 riblet heights. Increased resistance from improperly installed riblets is unfavorable in engineering applications and needs to be mitigated. It could be a valuable reference that the riblet should be more than 160 riblet heights away from the separation point.
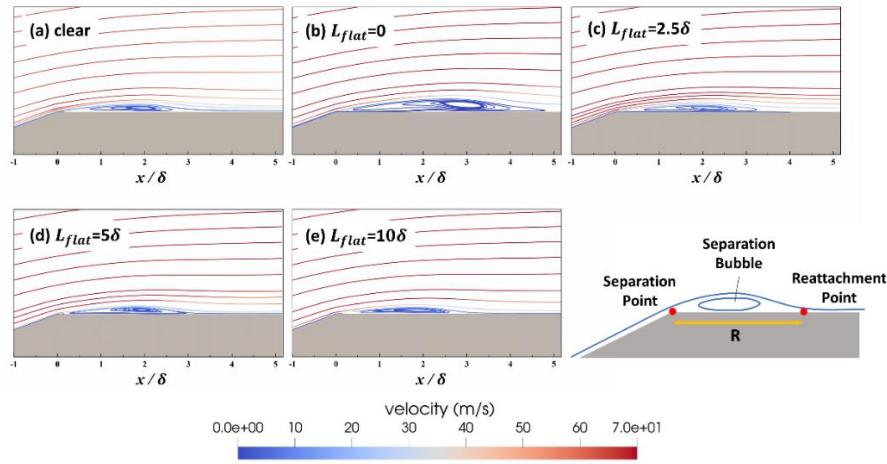
Figure 11: The time-averaged streamlines colored with velocity values at the mid-plane for (a) the case without riblet, (b) the case with L_{flat} of 0, (c) the case with L_{flat} of 2.5δ, (d) the case with L_{flat} of 5δ, (e) the case with L_{flat} of 10δ. In each case, the step angle is 20°.

15

Case	Riblet / Clear	Step angle θ	L_{flat} (δ)	C_d of step	Reattachment length R (δ)
9	Clear	20°	/	0.0716	2.94
10	Riblet	20°	0	0.0857	4.84
11	Riblet	20°	2.5	0.0745	3.85
12	Riblet	20°	5	0.0735	3.00
14	Riblet	20°	10	0.0716	2.95

Table 4: Reattachment length R for the 20-degree models with different L_{flat}.

4   Conclusions and Contributions

In this study, an inclined forward step model is proposed to investigate the interaction between riblet-induced drag reduction and upstream flow separation. Large eddy simulations were used to assess various step angles and riblet placements, revealing key insights into riblet behavior in separated flows—important for their use in high-speed train. The findings are:

1. **Riblets Reduce Frictional Resistance:** Despite upstream flow separation, riblets lower wall friction by dampening Reynolds stress near the wall. Quadrant analysis shows riblets suppress Q2 ejection motions in the turbulent layer.

2. **Enhanced Drag Reduction:** Riblets improve drag reduction, from 9.5% to 12.6%, with increasing step angles up to 30°. Quadrant analysis shows that with augmented flow separation, Q2 motion in the flow field increases, consequently elevating riblets' drag reduction capability.

3. **Pressure Drag and Riblet Positioning:** Pressure drag rises when riblets are near the separation point, promoting flow separation. A critical length, characterized by the riblet position (x/h), is identified, beyond which riblets' impact on separation is negligible, approximately 160 riblet heights.

The study's implications for riblet application in high Reynolds number flows are significant for train. However, the complexity of real-world vehicle surfaces and operational flow conditions presents challenges. Future work will model riblet performance to optimize simulation costs and conduct wind tunnel tests, advancing riblet technology for drag reduction in vehicles.

Acknowledgements

References

[1]   H. Choi, H. Park, W. Sagong, and S. Lee, 'Biomimetic flow control based on morphological features of living creatures', *Physics of Fluids*, vol. 24, no. 12, p. 121302, Dec. 2012, doi: 10.1063/1.4772063.

[2] M. Walsh, 'Turbulent boundary layer drag reduction using riblets', in *20th Aerospace Sciences Meeting*, Orlando,FL,U.S.A.: American Institute of Aeronautics and Astronautics, Jan. 1982. doi: 10.2514/6.1982-169.

[3] D. W. Bechert, M. Bruse, W. Hage, J. G. T. V. D. Hoeven, and G. Hoppe, 'Experiments on drag-reducing surfaces and their optimization with an adjustable geometry', *Journal of Fluid Mechanics*, vol. 338, pp. 59–87, May 1997, doi: 10.1017/S0022112096004673.

[4] P. Luchini, F. Manzo, and A. Pozzi, 'Resistance of a grooved surface to parallel flow and cross-flow', *Journal of Fluid Mechanics*, vol. 228, pp. 87–109, Jul. 1991, doi: 10.1017/S0022112091002641.

[5] S.-J. Lee and S.-H. Lee, 'Flow field analysis of a turbulent boundary layer over a riblet surface', *Experiments in Fluids*, vol. 30, no. 2, pp. 153–166, Feb. 2001, doi: 10.1007/s003480000150.

[6] H. Choi, P. Moin, and J. Kim, 'Direct numerical simulation of turbulent flow over riblets', *J. Fluid Mech.*, vol. 255, no. 1, p. 503, Oct. 1993, doi: 10.1017/S0022112093002575.

[7] D. Goldstein, R. Handler, and L. Sirovich, 'Direct numerical simulation of turbulent flow over a modeled riblet covered surface', *Journal of Fluid Mechanics*, vol. 302, pp. 333–376, Nov. 1995, doi: 10.1017/S0022112095004125.

[8] R. García-Mayoral and J. Jiménez, 'Drag reduction by riblets', *Philosophical Transactions of the Royal Society A: Mathematical, Physical and Engineering Sciences*, vol. 369, no. 1940, pp. 1412–1427, Apr. 2011, doi: 10.1098/rsta.2010.0359.

[9] P. R. Viswanath, 'Aircraft viscous drag reduction using riblets', *Progress in Aerospace Sciences*, vol. 38, no. 6–7, pp. 571–600, Aug. 2002, doi: 10.1016/S0376-0421(02)00048-9.

[10] M. Kurita *et al.*, 'Flight Test of a Paint-Riblet for Reducing Skin-Friction', in *2018 Applied Aerodynamics Conference*, American Institute of Aeronautics and Astronautics. doi: 10.2514/6.2018-3005.

[11] Y. Zhang, H. Chen, S. Fu, and W. Dong, 'Numerical study of an airfoil with riblets installed based on large eddy simulation', *Aerospace Science and Technology*, vol. 78, pp. 661–670, Jul. 2018, doi: 10.1016/j.ast.2018.05.013.

[12] K.-S. Choi, 'Effects of Longitudinal Pressure Gradients on Turbulent Drag Reduction with Riblets', in *Turbulence Control by Passive Means*, E. Coustols, Ed., in Fluid Mechanics and its Applications. Dordrecht: Springer Netherlands, 1990, pp. 109–121. doi: 10.1007/978-94-009-2159-7_7.

[13] T. V. Truong and Ph. Pulvin, 'Influence of wall riblets on diffuser flow', *Applied Scientific Research*, vol. 46, no. 3, pp. 217–227, Jul. 1989, doi: 10.1007/BF00404819.

[14] J. R. Debisschop and F. T. M. Nieuwstadt, 'Turbulent boundary layer in an adverse pressure gradient - Effectiveness of riblets', *AIAA Journal*, vol. 34, no. 5, pp. 932–937, 1996, doi: 10.2514/3.13170.

[15] S. Klumpp, M. Meinke, and W. Schröder, 'Numerical Simulation of Riblet Controlled Spatial Transition in a Zero-Pressure-Gradient Boundary Layer', *Flow Turbulence Combust*, vol. 85, no. 1, pp. 57–71, Jul. 2010, doi:

10.1007/s10494-010-9251-x.

[16] A. Boomsma and F. Sotiropoulos, 'Riblet drag reduction in mild adverse pressure gradients: A numerical investigation', *International Journal of Heat and Fluid Flow*, vol. 56, pp. 251–260, Dec. 2015, doi: 10.1016/j.ijheatfluidflow.2015.07.022.

[17] M. S. Darwish and F. H. Moukalled, 'Normalized Variable and Space Formulation Methodology for High-Resolution Schemes', *Numerical Heat Transfer, Part B: Fundamentals*, vol. 26, no. 1, pp. 79–96, Jul. 1994, doi: 10.1080/10407799408914918.

[18] F. Nicoud and F. Ducros, 'Subgrid-Scale Stress Modelling Based on the Square of the Velocity Gradient Tensor', *Flow, Turbulence and Combustion*, vol. 62, no. 3, pp. 183–200, Sep. 1999, doi: 10.1023/A:1009995426001.

[19] O. Ben-Nasr, A. Hadjadj, A. Chaudhuri, and M. S. Shadloo, 'Assessment of subgrid-scale modeling for large-eddy simulation of a spatially-evolving compressible turbulent boundary layer', *Computers & Fluids*, vol. 151, pp. 144–158, Jun. 2017, doi: 10.1016/j.compfluid.2016.07.004.

[20] M. Weickert, G. Teike, O. Schmidt, and M. Sommerfeld, 'Investigation of the LES WALE turbulence model within the lattice Boltzmann framework', *Computers & Mathematics with Applications*, vol. 59, no. 7, pp. 2200–2214, Apr. 2010, doi: 10.1016/j.camwa.2009.08.060.

[21] L. Temmerman, M. A. Leschziner, C. P. Mellen, and J. Fröhlich, 'Investigation of wall-function approximations and subgrid-scale models in large eddy simulation of separated flow in a channel with streamwise periodic constrictions', *International Journal of Heat and Fluid Flow*, vol. 24, no. 2, pp. 157–180, Apr. 2003, doi: 10.1016/S0142-727X(02)00222-9.

[22] S. Jee, J. Joo, and G. Medic, 'Large-Eddy Simulation of a High-Pressure Turbine Vane With Inlet Turbulence', presented at the ASME Turbo Expo 2016: Turbomachinery Technical Conference and Exposition, American Society of Mechanical Engineers Digital Collection, Sep. 2016. doi: 10.1115/GT2016-56980.

[23] G. Medic, V. Zhang, G. Wang, J. Joo, and O. P. Sharma, 'Prediction of Transition and Losses in Compressor Cascades Using Large-Eddy Simulation', *Journal of Turbomachinery*, vol. 138, no. 12, p. 121001, Dec. 2016, doi: 10.1115/1.4033514.

[24] S. Qin, M. Koochesfahani, and F. Jaberi, 'Large eddy simulations of unsteady flows over a stationary airfoil', *Computers & Fluids*, vol. 161, pp. 155–170, Jan. 2018, doi: 10.1016/j.compfluid.2017.11.014.

[25] J. M. Wallace, 'Quadrant Analysis in Turbulence Research: History and Evolution', *Annu. Rev. Fluid Mech.*, vol. 48, no. 1, pp. 131–158, Jan. 2016, doi: 10.1146/annurev-fluid-122414-034550.

[26] A. M. Akbarzadeh and I. Borazjani, 'Reducing flow separation of an inclined plate via travelling waves', *Journal of Fluid Mechanics*, vol. 880, pp. 831–863, Dec. 2019, doi: 10.1017/jfm.2019.705.

[27] T. J. Mueller, 'Aerodynamics of Small Vehicles', *Annual Review of Fluid Mechanics*, vol. 35, pp. 89–111, Jan. 2003, doi: 10.1146/annurev.fluid.35.101101.161102.